Article:
Stefanek, P. orcid.org/0000-0002-8581-1309, Synek, A., Dall'Ara, E. orcid.org/0000-0003-1471-5077 et al. (1 more author) (2023) Comparison of linear and nonlinear stepwise μFE displacement predictions to digital volume correlation measurements of trabecular bone biopsies. Journal of the Mechanical Behavior of Biomedical Materials, 138. 105631. ISSN 1751-6161

https://doi.org/10.1016/j.jmbbm.2022.105631

journal of the mechanical behavior of biomedical materials 138 (2023) 105631

Contents lists available at ScienceDirect

Journal of the Mechanical Behavior of Biomedical Materials

journal homepage: www.elsevier.com/locate/jmbbm

Comparison of linear and nonlinear stepwise μFE displacement predictions to digital volume correlation measurements of trabecular bone biopsies

Pia Stefanek [a,*], Alexander Synek [a], Enrico Dall'Ara [b], Dieter H. Pahr [a,c]

[a] Institute of Lightweight Design and Structural Biomechanics, TU Wien, Austria
[b] Department of Oncology and Metabolism and Insigneo Institute for in Silico Medicine, University of Sheffield, UK
[c] Division Biomechanics, Karl Landsteiner University of Health Sciences, Austria

ARTICLE INFO

Keywords:
Micro finite element model
Materially nonlinear simulation
Digital volume correlation
Displacement
Trabecular bone biopsies

ABSTRACT

Digital volume correlation (DVC) enables to evaluate the ability of μFE models in predicting experimental results on the mesoscale. In this study predicted displacement fields of three different linear and materially nonlinear μFE simulation methods were compared to DVC measured displacement fields at specific load steps in the elastic regime ($Step_{El}$) and after yield ($Step_{Ult}$). Five human trabecular bone biopsies from a previous study were compressed in several displacement steps until failure. At every compression step, μCT images (resolution: 36 μm) were recorded. A global DVC algorithm was applied to compute the displacement fields at all loading steps. The unloaded 3D images were then used to generate homogeneous, isotropic, linear and materially nonlinear μFE models. Three different μFE simulation methods were used: linear (L), nonlinear (NL), and nonlinear stepwise (NLS). Regarding L and NL, the boundary conditions were derived from the interpolated displacement fields at $Step_{El}$ and $Step_{Ult}$, while for the NLS method nonlinear changes of the boundary conditions of the experiments were captured using the DVC displacement field of every available load step until $Step_{El}$ and $Step_{Ult}$. The predicted displacement fields of all μFE simulation methods were in good agreement with the DVC measured displacement fields (individual specimens: R^2>0.83 at $Step_{El}$ and R^2>0.59 at $Step_{Ult}$; pooled data: R^2>0.97 at $Step_{El}$ and R^2>0.92 at $Step_{Ult}$). At $Step_{El}$, all three simulation methods showed similar intercepts, slopes, and coefficients of determination while the nonlinear μFE models improved the prediction of the displacement fields slightly in all Cartesian directions at $Step_{Ult}$ (individual specimens: L: R^2>0.59 and NL, NLS: R^2>0.68; pooled data: L: R^2>0.92 and NL, NLS: R^2>0.94). Damaged/overstrained elements in L, NL, and NLS occurred at similar locations but the number of overstrained elements was overestimated when using the L simulation method. Considering the increased solving time of the nonlinear μFE models as well as the acceptable performance in displacement prediction of the linear μFE models, one can conclude that for similar use cases linear μFE models represent the best compromise between computational effort and accuracy of the displacement field predictions.

1. Introduction

Bone has a complex, hierarchical structure that spans multiple length scales (Rho et al., 1998). Since all scales are contributing to the mechanical behaviour of bone, understanding bone failure still remains challenging. Especially research concerning the link between failure mechanisms of bone acting at different length scales is still incomplete (Sabet et al., 2016).

Over the past 30 years, with the increase of computational power and the improvement of imaging techniques, computational modelling has been established as a popular tool to non-invasively predict the mechanical properties and failure processes of bone (Bevill and Keaveny, 2009; Cody et al., 1999; van Rietbergen et al., 1995; Yeh and Keaveny, 2001). Due to tremendous improvement in resolution, micro computed tomography (μCT) scanners are nowadays able to capture the bone architecture at the micro scale (~30 μm resolution) and even below. For this reason, micro finite element (μFE) models represent a non-invasive addition to lab-experiments to investigate the mechanical behaviour of bone under loading at the microscale. In most micro finite element (μFE) studies so far, bone is modelled using a linear-elastic material law (Boyd, 2009; Müller, 2009; Ruffoni and van Lenthe, 2011; van Rietbergen and Ito, 2015). But such analyses cannot be used

* Corresponding author. Gumpendorfer Straße 7, A-1060, Wien, Austria.
E-mail address: stefanek@ilsb.tuwien.ac.at (P. Stefanek).

https://doi.org/10.1016/j.jmbbm.2022.105631
Received 21 June 2022; Received in revised form 30 November 2022; Accepted 15 December 2022
Available online 22 December 2022

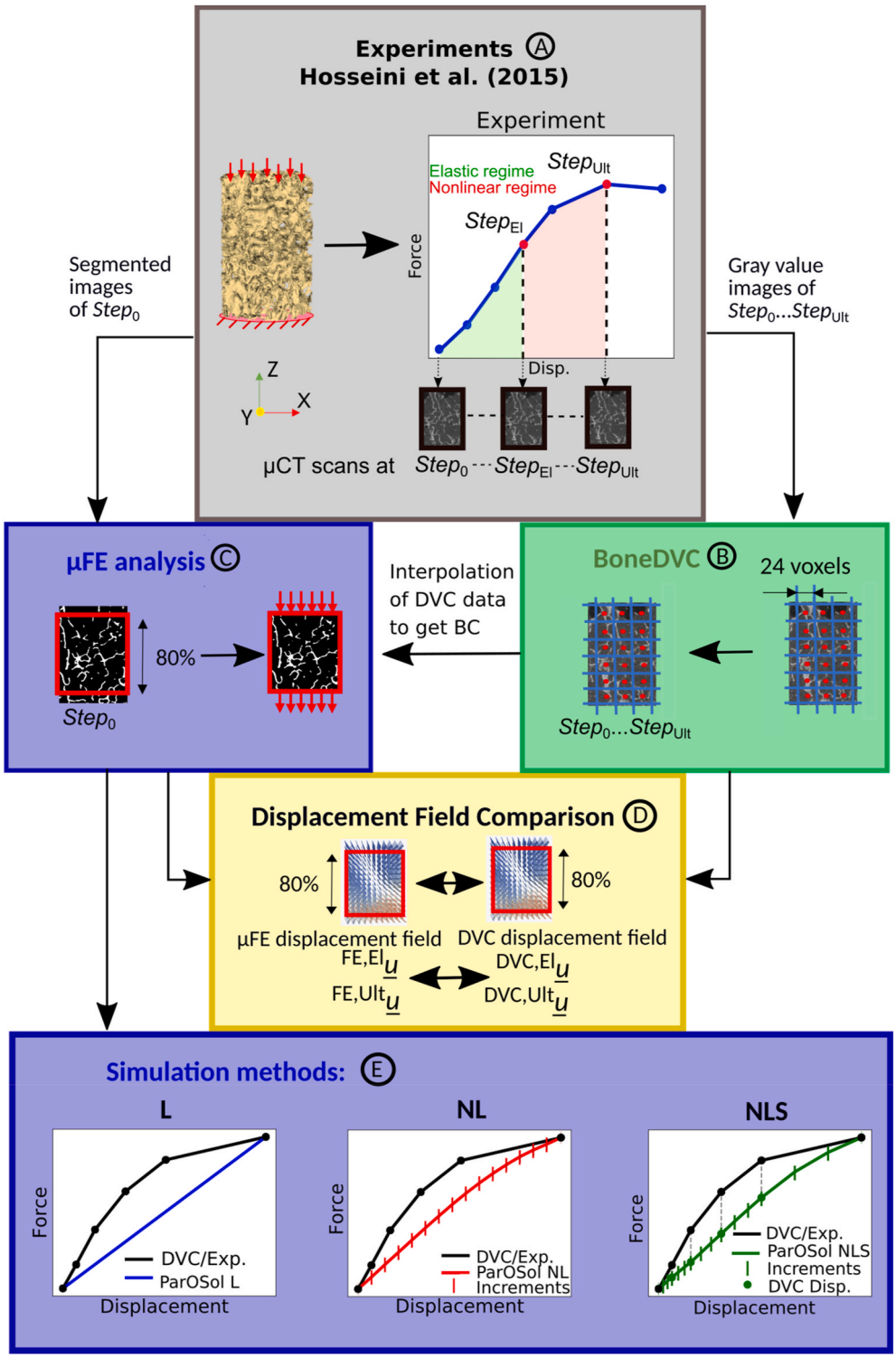

Fig. 1. Complete workflow of the study. A. Stepwise compression experiments from Hosseini et al. (2015). B. Application of BoneDVC algorithm on the gray value images. C. μFE analyses of the middle 80% of the preloaded segmented images. D. Displacement field comparison: μFE predicted vs. DVC measured. Only the middle 80% of the μFE models were evaluated corresponding to 64% of the original specimen height. E. Overview of the simulation methods: L, NL, and NLS.

to simulate deformations beyond the elastic limit, which occur for example when bone fractures. In order to predict failure behaviour, a nonlinear material law is required.

Since bone exhibits several mechanisms such as plasticity, damage, viscosity, and creep in the post-yield regime, a wide range of different constitutive models have been developed (Sabet et al., 2018; Schwiedrzik et al., 2016; Stipsitz et al., 2020). Each of these models is formulated for a limited range of applications (e.g. trabecular/cortical bone, whole bone/single trabeculae, small/large strain, etc.) in which it is capable to replicate the real mechanical behaviour with acceptable accuracy (Pahr and Reisinger, 2020). However, a tradeoff between computational efficiency and the complexity of the implemented material model must be found to enable feasible runtimes of the μFE simulations. Most general-purpose FE solvers (e.g. Abaqus, Ansys) are able

to account for different types of nonlinearity (geometric (Verhulp et al., 2008), material (Niebur et al., 2000) and contact nonlinearity (Ovesy et al., 2019)) but are only a viable option for model sizes up to a few millions of elements. For example, Ding et al. (2008) needed 310 CPU hours to solve a nonlinear simulation of a trabecular bone model with 0.7million elements with Abaqus/Standard. Increasing model sizes further raise computational requirements and make the use of a supercomputer essential. Highly specialized software generated to solve large-scale problems (e.g. FEAP (Taylor, 2014), Faim (Numerics88 Solutions Ltd, https://bonelab.github.io/n88/index.html), ParOSol (Flaig and Arbenz, 2012), ParOSol-NL (Stipsitz et al., 2020)) have better parallel execution performance but are generally based on linear-elastic or very simple nonlinear material models. For example, ParOSol-NL is able to solve even very large nonlinear models with up to a few hundreds of million elements in approximately 5500 CPU hours (Stipsitz and Pahr, 2018).

Before their application, the μFE models have to be validated against accurate experimental measurements. For instance, apparent properties (e.g. stiffness, strength) can be compared directly to experimental measurements from standard monotonic mechanical testing (Christen et al., 2013; Stipsitz et al., 2020, 2021; Wolfram et al., 2010). Experimental validation of local predictions was recently made possible by using Digital Volume Correlation (DVC). Given μCT images of the unloaded and the loaded specimens, DVC is able to measure the 3D displacement field, which can be compared to the μFE model predicted displacement field. However, for image resolutions of about 30 μm the DVC displacement field is typically measured in a regular grid with a specific spacing of approximately 0.5–2 mm (Dall'Ara et al., 2017). Thus, "local" displacements typically define displacements of volumes of this size which is rather a meso than a micro quantity.

In the last years, DVC was successfully applied multiple times to get more insight into strain distributions (Palanca et al., 2021; Ryan et al., 2020) and fracture patterns (Jackman et al., 2016; Martelli et al., 2021; Yan et al., 2020) of bone. Furthermore, several studies evaluated the agreement between FE predicted displacements and DVC measured displacements in the elastic and in the nonlinear regime. Zauel et al. (2006) showed an excellent correlation in μFE displacements of cancellous uniaxially loaded bone biopsies only in axial loading direction while other studies reported excellent agreements with DVC data in all directions (R^2>0.86) (Chen et al., 2017; Costa et al., 2017). In a recent study, very good agreement has been found between μFE and DVC displacements for very complex vertebral bodies with induced focal lesions (R^2>0.84) (Palanca et al., 2022). Oliviero et al. (2018) were able to replicate the DVC displacement field in the nonlinear regime using linear μFE models (R^2>0.76). Jackman et al. (2016) compared predicted displacements of nonlinear quantitative computed tomography (QCT) based FE models to DVC measured displacements in the nonlinear regime. The correlation results were only moderate with coefficients of determination ranging between 0.06 and 0.77. Madi et al. (2013) applied a nonlinear material model to a scaffold implant material made of 85:15 poly(D,L-lactide-*co*-glycolide) and were able to replicate the displacement field up to 3% strain. To the author's knowledge, only one recent study has yet compared displacements predicted by nonlinear μFE to DVC measured displacements in bone. Peña Fernández et al. (2022) successfully replicated the DVC displacement field (R^2>0.79) up to 3% nominal strain. Their μFE models were solved with the commercial solver Abaqus/Standard with the benefit of a complex material law including geometrical nonlinearity and the drawback of low computational efficiency.

The aim of this study was to compare the displacement predictions of three different linear and materially nonlinear μFE simulation methods using the highly efficient μFE solver ParOSol-NL in both pre- and post-yield loading stages. To examine the validity of the predicted displacement fields, their agreement to DVC displacements measured from compressive tests of human trabecular bone biopsies was evaluated.

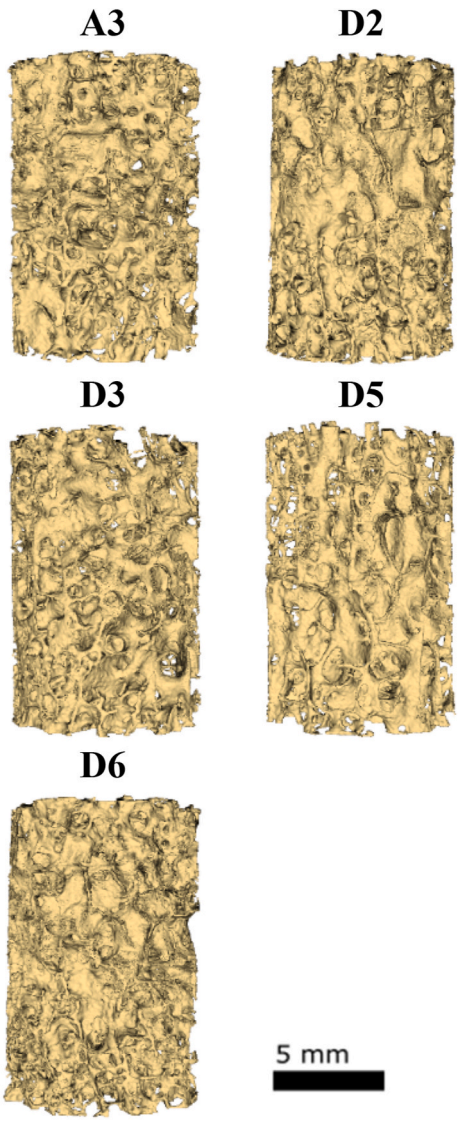

Fig. 2. 3D representation of the five selected human trabecular bone biopsies A3 to D6.

2. Materials and methods

Fig. 1 shows the outline of this study. In brief, human trabecular bone biopsies from a previous study were compressed in several displacement steps until failure. At every loading step, μCT images were recorded. A non-rigid registration was applied to the images to get the displacement fields at all loading steps until failure. The unloaded 3D images were then used to generate linear and materially nonlinear μFE models. Three different μFE simulation methods were compared: linear (L), nonlinear (NL), and nonlinear stepwise (NLS). Finally, the displacement fields predicted by the μFE models were compared to the DVC displacement fields at a specific load step in the elastic regime and at the ultimate load step.

2.1. Experimental data

The study is based on experimental data of five randomly selected human trabecular bone biopsies (see Fig. 2) which were used in a previous study (Hosseini et al., 2015). The five selected cylindrical biopsies, which were extracted from the thoracic and lumbar spine, measured about 11 mm in height and 8 mm in diameter and had a mean relative bone volume fraction (BV/TV) of 14%. Their morphometrics were

Table 1
Dimensions and morphometrics of the five bone specimens (A3-D6) used in this study.

Specimen ID	Diameter in mm	Height in mm	BV/TV in %	Tb.N in 1/mm	Tb.Th[a] in µm	Tb.Sp[a] in µm
A3	8.1	11.556	13.6	0.85	181 ± 45	1002 ± 402
D2	8.172	11.88	19.9	1.04	181 ± 51	783 ± 279
D3	8.064	11.592	11.3	0.8	178 ± 45	1067 ± 414
D5	8.064	11.808	8.6	0.68	181 ± 48	1285 ± 511
D6	8.064	11.808	16.7	0.99	174 ± 40	832 ± 306

Note: bone volume fraction (BV/TV), trabecular number (Tb.N), trabecular thickness (Tb.Th), trabecular separation (Tb.Sp).
[a] Mean ± standard deviation.

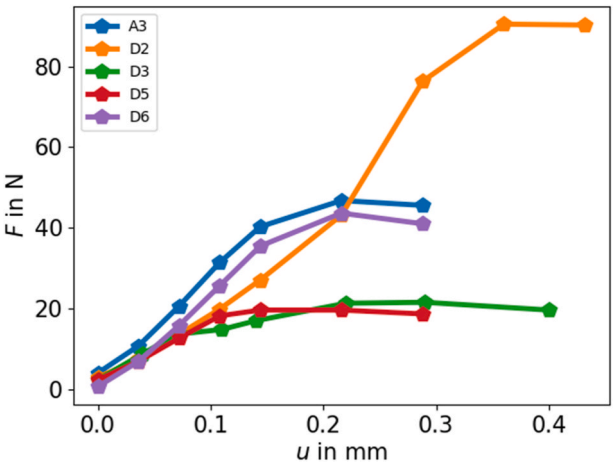

Fig. 3. Experimental force-displacement curves of all analyzed specimens A3 to D6. The given force values describe the forces after relaxation.

evaluated with the software Medtool (v4.5, Dr. Pahr Ingenieurs e.U., Pfaffstätten, Austria) (Table 1). In the original study, nominal uniaxial compression experiments were performed on each specimen using a custom loading device inside a SCANCO µCT 40 (SCANCO Medical AG, Brüttisellen, Schweiz) machine (see Fig. 1A). An axial load was applied manually using a screw and was measured with a loadcell (HBM Type C9B 2 kN). While the samples' bottom surface was fixed using epoxy glue to ensure fully clamped boundary conditions, the top surface of the samples was glued to a uniaxially moving part. Displacement-controlled loading was applied in a stepwise manner (nominal displacement step size: 0.03mm–0.072 mm) until failure. The specimens were scanned in the preloaded configuration (1–4N) and at every loading step with a resolution of 36 µm. In order to reduce relaxation-effects during the scan, the µCT image acquisition was started approximately 30min after load application. The scanning parameters were: voltage of 70000V, current of 114 µA, projection number of 250 and exposure time of 200 ms. Compared to the original study, only steps until a drop of force were considered (see Fig. 1A $Step_{Ult}$). The number of used loading steps varied between five and seven. At $Step_{Ult}$, the specimens reached loads between 21.6N and 90.48N and were compressed with apparent strain from 1.8% to 3% (see Fig. 3). In addition to the gray value images obtained from the µCT scanning also segmented images of every loading step were available from the previous study (Hosseini et al., 2015). They were generated by applying single level thresholding on the smoothed (Gauss filter with $\sigma = 0.8$ and a kernel size of $3 \times 3 \times 3$) gray-value images.

2.2. Digital volume correlation

The DVC displacement field of every loading step was computed over the entire volume using a global DVC algorithm (BoneDVC, https://bonedvc.insigneo.org/dvc/) (see Figs. 1B and 4). Details about the algorithm are reported in multiple publications (Dall'Ara et al., 2017, 2014; Palanca et al., 2015). Briefly, a cubic grid with a selected grid spacing (GS) (previously referred to as nodal spacing (NS) in Dall'Ara et al. (2014) and other literature) is superimposed on the 3D gray value images. Then, elastic registration is applied to the preloaded and deformed images using the Sheffield Image Registration Toolkit (ShIRT). The software solves the registration equations at the nodes of the grid using trilinear interpolation between the nodes. In this study a GS of 24 voxels (0.864 mm) was selected following previous studies that used the same global DVC approach on µCT images of bone with similar scanning resolutions, which reported displacement precision below 2.5 µm (Knowles et al., 2019; Kusins et al., 2019; Tozzi et al., 2017). In order to exclude boundary effects of the experiment only the middle 80% of the DVC displacement field were considered for further processing. Boundary effects arise from artefacts of the experimental setup and can lead to high measurement errors in the regions close to the boundary. Since this effect diminishes farther away from the boundary, a general practice is to exclude the edge parts from the experimental evaluation (Costa et al., 2017; Oliviero et al., 2018; Palanca et al., 2022).

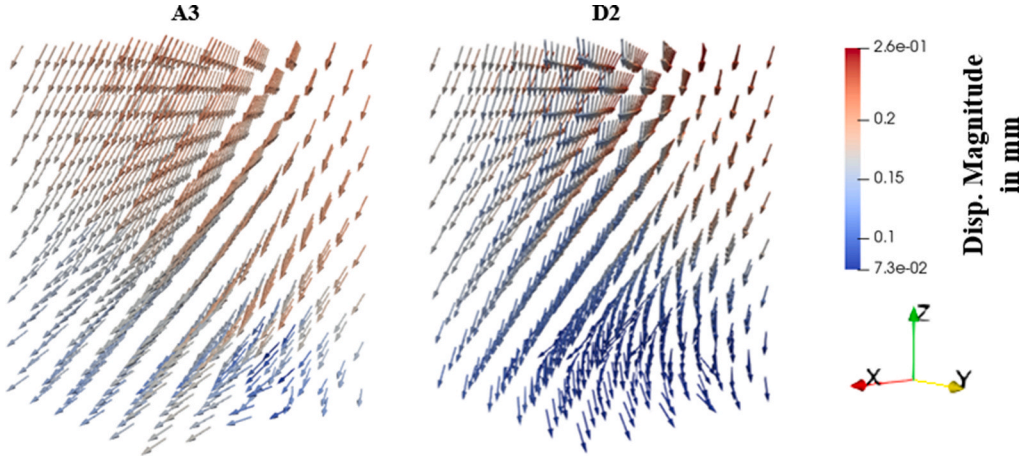

Fig. 4. 3D representation of the DVC measured displacement field at the ultimate load step of two representative specimens (A3 and D2).

Table 2
Comparison of element number, degrees of freedom and computational costs in CPU hours for all simulation methods and all specimens at $Step_{Ult}$.

Specimen	Element number in million	DoF in million	CPU hours at $Step_{Ult}$		
			L[a]	NL[a]	NLS[b]
A3	13.0	39.5	0.9	60.7	177.4
D2	13.6	41.3	0.7	51.4	193.7
D3	12.9	39.2	1.0	98.5	230.8
D5	13.2	40.0	1.0	91.1	213.4
D6	13.2	40.0	1.1	68.5	182.9

[a] Usage of 72CPUs.
[b] Usage of 80CPUs.

2.3. μFE modelling

The segmented μCT images of each specimen were cropped (middle 80% of height) and μFE models were created from the images in the preloaded configuration (see Fig. 1C). All voxels were converted into 8-noded hexahedral elements and isotropic, homogeneous material properties were assigned. According to Stipsitz et al. (2020) an elastic modulus of $E_0 = 10$ GPa was selected for the bone voxels but it was reduced to $E_0 = 2$ GPa in order to account for the stress relaxation during the stepwise loading experiment (Hosseini et al., 2015). Note that the selected value for E_0 is not relevant in this study, since only displacements and not forces are considered. The Poisson's ratio of the bone voxels was selected to be $\nu = 0.3$ (Stipsitz et al., 2020, 2021). Depending on the simulation method, linear-elastic or damage-based nonlinear material properties were chosen. The used nonlinear material model consists of a linear-elastic region, a damaged region including hardening (hardening modulus $E_h = 0.05E_0$) and a failure region. The material degradation in the damaged region is modelled by reduction of the elastic modulus dependent on the observed damage. An isotropic, quadric damage onset surface models the transition from the linear-elastic to the nonlinear regime (shape parameter $\zeta_0 = 0.3$, critical damage $D_c = 0.9$) (Stipsitz et al., 2020, 2021). Different damage onset strains in tension and compression ($\varepsilon_0^+ = 0.0068$, $\varepsilon_0^- = 0.0089$) are used to account for the tension-compression asymmetry of bone (Stipsitz et al., 2020, 2021). In order to capture also deformations of the void volume, background voxels were assigned linear-elastic material properties with an elastic modulus of $E_0 = 0.0002$ GPa and a Poisson's ratio of $\nu = 0.3$. Displacement boundary conditions were applied to the top and bottom layers of the μFE models. The boundary conditions were obtained by trilinear interpolation of the DVC derived displacement fields at a prior defined elastic load step (${}^{DVC,\,El}\underline{u}$) and at $Step_{Ult}$ (${}^{DVC,\,Ult}\underline{u}$) following the methodology of Chen et al. (2017). In order to define the elastic load step ($Step_{El}$) the 0.1% strain-offset method was used to determine the yield point of the experimental force-displacement curves. The last load step before yield was defined to be $Step_{El}$. For every specimen six different μFE models were created to predict the displacement fields at the elastic and at the ultimate load step for three different simulation methods (see next section).

2.4. Simulation methods

In this study three different simulation methods were compared (see Fig. 1E): linear (L), nonlinear (NL), and nonlinear-stepwise (NLS). For the L method, linear-elastic material properties were assigned to the bone voxels. The boundary conditions were derived from DVC displacement fields ${}^{DVC,\,El}\underline{u}$ and ${}^{DVC,\,Ult}\underline{u}$. The DVC displacement fields were obtained by single registration of the preloaded to the deformed images at $Step_{El}/Step_{Ult}$ without considering any in-between steps. The linear μFE analysis was solved in one increment. For the NL simulation method, damage-based nonlinear material properties were applied and the analysis was solved in several displacement increments of same size i.e. the DVC displacement at the boundary was taken (${}^{DVC,\,El}\underline{u}$, ${}^{DVC,\,Ult}\underline{u}$) and linearly scaled in-between (radial load). Regarding the NLS method, the boundary conditions were applied stepwise using the DVC displacement field of every available load step until $Step_{El}$ and $Step_{Ult}$. In order to obtain all of these displacement fields the preloaded images had to be registered to the deformed images of all in-between load steps until $Step_{El}/Step_{Ult}$. Note that the NLS method therefore also captures nonlinear changes of the boundary conditions of the experiments (non-radial load), which might affect the damage evolution and hence influence the prediction of the displacements (see Fig. 1E).

All μFE models were solved with the μFE solver ParOSol-NL (Stipsitz et al., 2020) on a cluster using up to 80 CPUs (CPU: AMD Ryzen 7 3700X). The number of elements ranged between 12.9million and 13.6million (see Table 2). Furthermore, Table 2 lists the CPU hours for all simulation methods and specimens at $Step_{Ult}$.

2.5. Comparison between μFE and DVC and damage analysis

In order to reduce boundary condition effects, only the middle 80% in height of the μFE models (corresponding to 64% in height of the

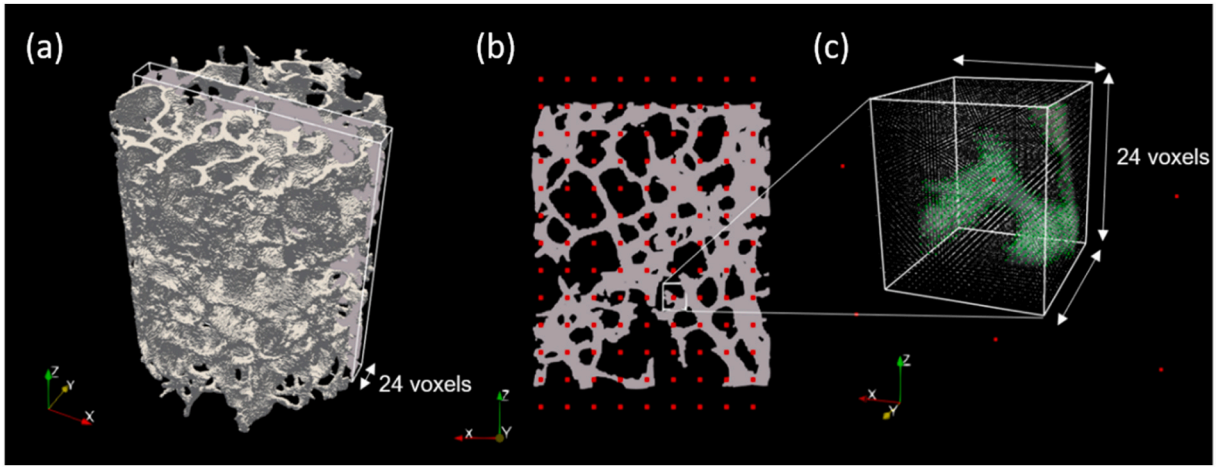

Fig. 5. Graphical description of the volume averaging method. (a) Shows the whole bone biopsy. A small part in the middle with a thickness of 24 voxels is cut out and shown in (b). In (b) the sliced bone overlaid by the DVC points marked in red is displayed. (c) Focusses on a single cube with 24 voxels surrounding one DVC point. The DVC point in the middle of the cube is again marked in red, while μFE mesh nodes corresponding to bone material are displayed in green and μFE mesh nodes corresponding to bone marrow material are visualized in white. To compare the DVC displacement with the μFE predicted displacement the nodal displacements of all nodes within the corresponding 24 × 24 × 24 voxel cube were averaged.

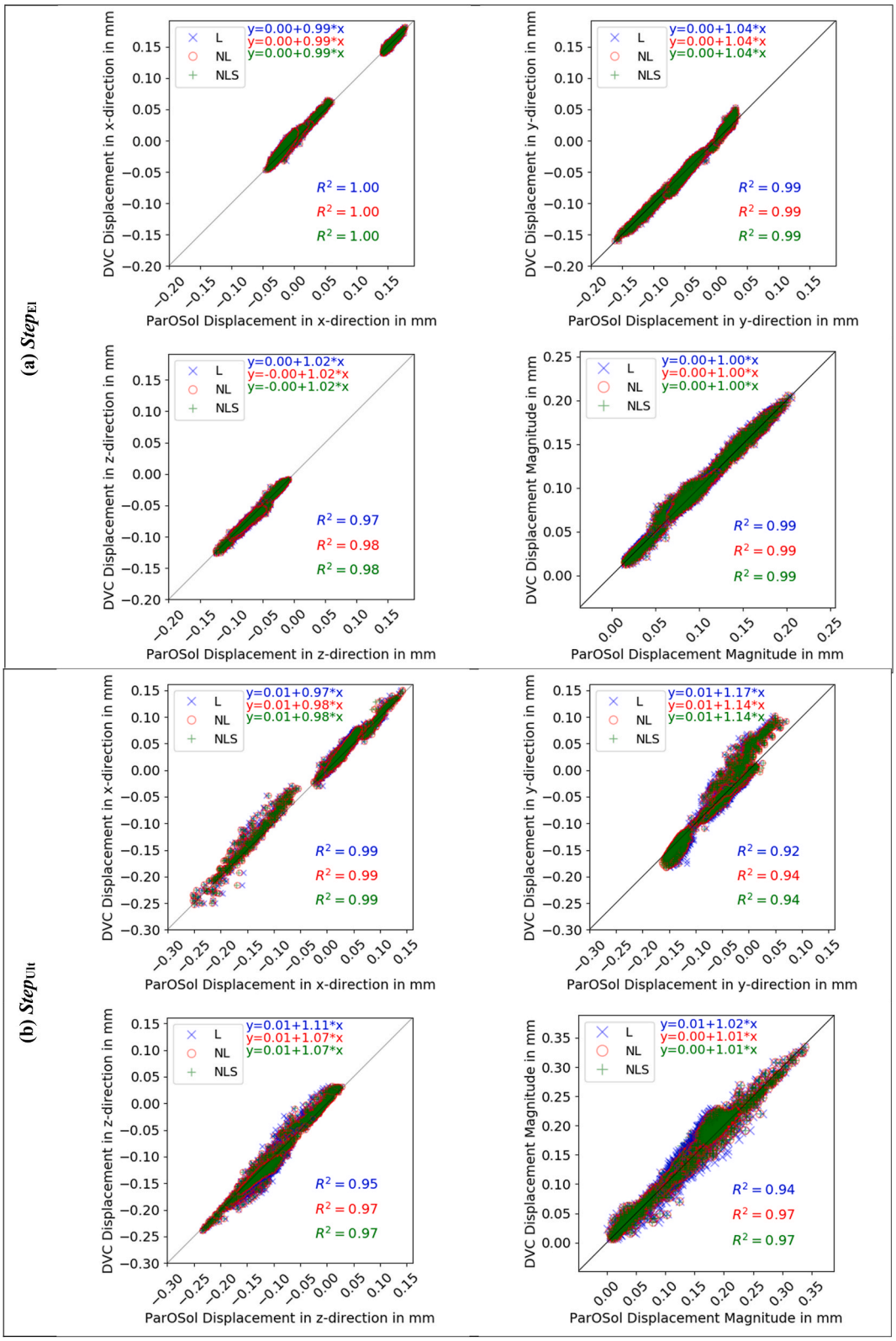

Fig. 6. Linear regression analyses of pooled data between the μFE predicted displacements and the DVC measured displacements for all 5 specimens at the elastic (a) and at the ultimate (b) load step.

original specimens) were considered for comparing the predicted and measured displacement fields. The comparison was performed at $Step_{El}$ ($^{FE,\ El}\underline{u}$ vs. $^{DVC,\ El}\underline{u}$) and at $Step_{Ult}$ ($^{FE,\ Ult}\underline{u}$ vs. $^{DVC,\ Ult}\underline{u}$) (see Fig. 1D).

A so-called volume-averaging method, similar to the method used by Fu et al. (2021), was applied to compare the displacement fields (see Fig. 5 and Appendix A) instead of a pointwise comparison (Chen et al., 2017; Costa et al., 2017). The complete FE mesh was superimposed by the cubic grid used to perform the DVC registration. Hence, every node in the FE mesh was included in a cube of 24 × 24 × 24 voxels in size and a DVC point in the middle. All nodes in a specific cube were then

Table 3
Minimum coefficient of determination (R^2) of all three spatial directions of individual specimens.

Min(R_x^2, R_y^2, R_z^2)		A3	D2	D3	D5	D6
(a) $Step_{El}$	**L**	0.92	0.96	0.89	0.83	0.88
	NL	0.92	0.96	0.89	0.85	0.88
	NLS	0.92	0.96	0.89	0.85	0.88
(b) $Step_{Ult}$	**L**	0.66	0.93	0.89	0.87	0.59
	NL	0.73	0.95	0.92	0.88	0.68
	NLS	0.73	0.95	0.92	0.88	0.68

assigned to the corresponding DVC point. The displacements of all nodes inside a specific cube were then averaged (including both bone and void volume) and compared to the corresponding displacement value of the DVC point. DVC points inside a surrounding cubic volume with a relative density lower than 5% were excluded from the displacement field comparison. Furthermore, DVC points located outside of the bone cylinder were not considered.

Linear regressions were used to show the relationship between the measured DVC displacement fields and the μFE predicted displacement fields. For each specimen, for both relevant load steps ($Step_{El}$, $Step_{Ult}$), for all three Cartesian components of the displacement field and for its magnitude, the following parameters were computed: Slope, intercept, coefficient of determination (R^2), residuals, and root mean square error (RMSE). Furthermore, the spatial distribution of the residuals was evaluated qualitatively. For this purpose, all μFE mesh nodes of a specific cube surrounding a DVC point were assigned the corresponding residual value ($^{FE}\underline{u}$ - $^{DVC}\underline{u}$) of that DVC point. Nodes in volumes where the DVC point was excluded were displayed in black colour.

Damage was evaluated at $Step_{Ult.}$ Regarding the L simulation method an element was classified as damaged if the effective strain ε_{eff} exceeded a critical value of $\varepsilon_c = 0.89\%$ (Stipsitz et al., 2021). This value was selected since it corresponded to the yield strain in compression of the material model used for NL and NLS.

For the simulation methods NL and NLS an element was defined as damaged if damage $D > 0$. Damage evolution was compared for NL and NLS for the apparent strain value ε of the cropped specimen (80% of original height).

All statistical evaluations were performed using Python 3.8 (https://www.python.org/) and the included library SciPy (Virtanen et al., 2020). All figures showing the spatial distribution of residuals and the distribution of damage were created using Paraview (https://www.paraview.org/).

3. Results

3.1. Correlation of displacement fields

The evaluation of displacement fields of all specimens at $Step_{El}$ ($^{FE,\,El}\underline{u}$ vs. $^{DVC,\,El}\underline{u}$) showed that μFE model displacements were highly correlated to DVC displacements (R^2 between 0.97 and 1 for pooled data and R^2>0.83 for individual specimens) (see Fig. 6 (a), Table 3 (a) and

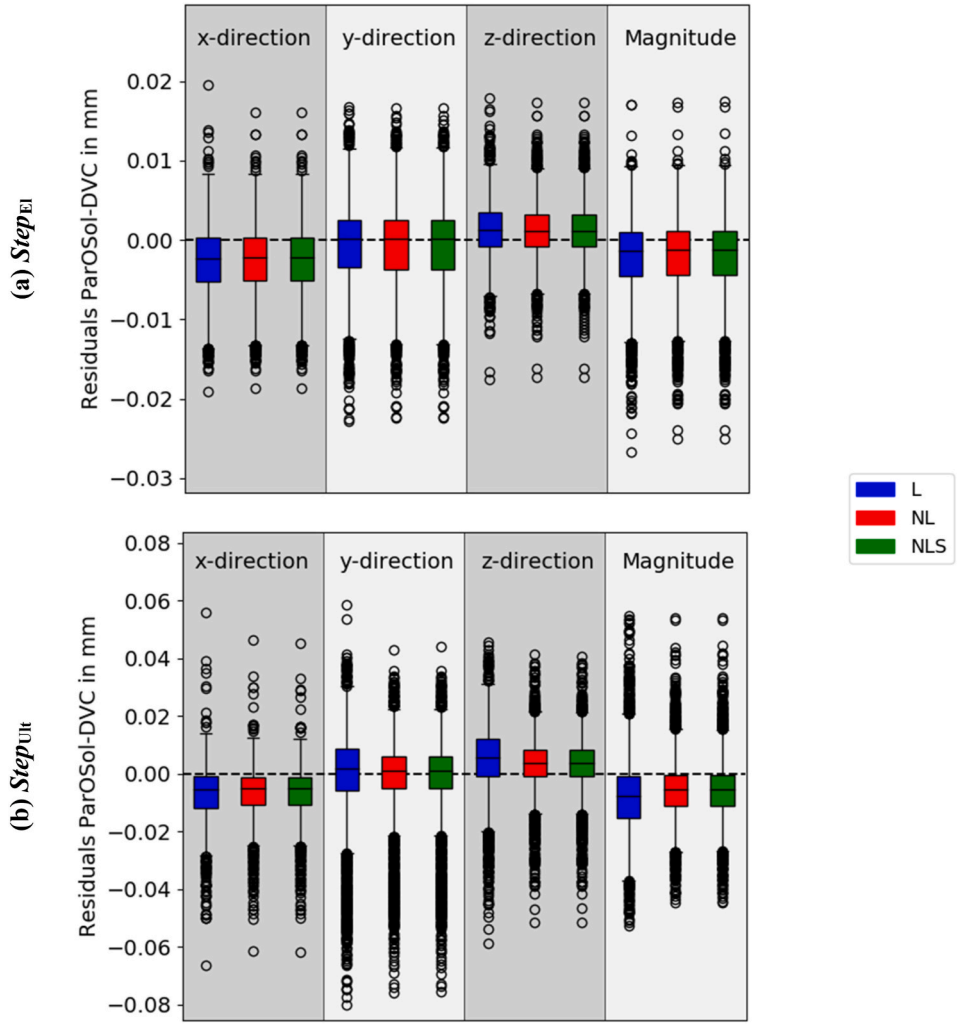

Fig. 7. Boxplot of residuals of pooled data of all specimens at the elastic (a) and at the ultimate (b) load step.

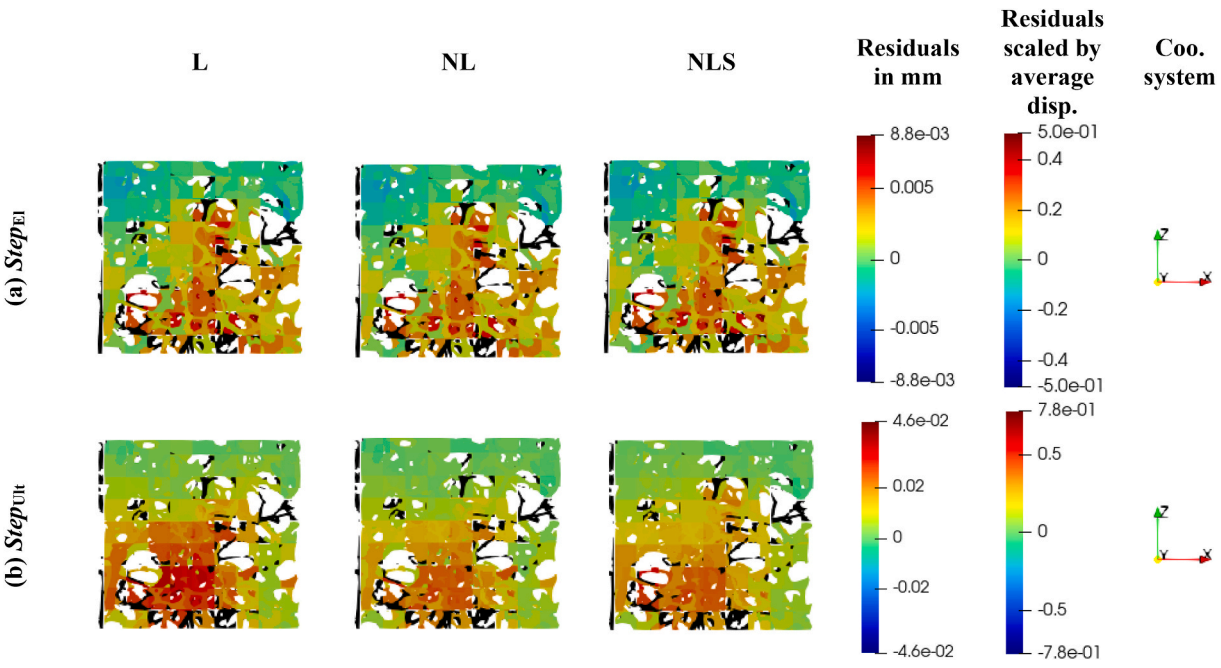

Fig. 8. Spatial distribution of residuals at the elastic (a) and at the ultimate (b) load step of one representative specimen (A3) in z-direction. All bone material nodes of a specific volume were assigned to the corresponding residual value of the specific DVC point. Nodes in volumes where the DVC point was excluded were displayed in black colour. Two colour maps were used: One shows the residuals in mm and the other one scales the residual value with the average compression of the specimen (see Appendix B).

supplementary material). Intercepts were close to zero and slopes close to one for all methods and all Cartesian coordinates and magnitude (Intercept: -0.2 μm–3.2 μm; Slope: 0.99 to 1.04 for pooled data). Regarding intercept, slope, and R^2, all three simulation methods showed similar results.

Similar to the results at $Step_{El}$ the evaluation of displacement fields of all specimens at $Step_{Ult}$ ($^{FE,\ Ult}\underline{u}$ vs. $^{DVC,\ Ult}\underline{u}$) showed a high correlation between μFE model displacements and DVC displacements (see Fig. 6 (b), Table 3 (b) and supplementary material). For pooled data, intercepts were close to zero (4.4 μm–12 μm) and slopes ranged between 0.97 and 1.17. In all spatial directions and for the magnitude, slopes and R^2 values were closer to one for the simulation methods NL and NLS (R^2>0.94 for pooled data and R^2>0.68 for individual specimens) compared to L (R^2>0.92 for pooled data and R^2>0.59 for individual specimens). Furthermore, the intercept values for NL and NLS were closer to zero and slopes closer to one in comparison to L. No difference was observed between NL and NLS.

3.2. Residuals

At $Step_{El}$, the residuals showed similar interquartile range (IQR), medians and residual ranges for all methods (see Fig. 7 (a)). When all directions are considered, the residuals ranged from −22μm to 20 μm.

At $Step_{Ult}$, IQR and residual ranges were slightly higher for the simulation method L in all directions and for the magnitude (e.g. z-direction: Residual range of L: -59 μm–46 μm; Residual range of NL and NLS: -52 μm–41 μm) (see Fig. 7 (b)). Furthermore, the median was shifted further from zero for L (e.g. z-direction: Median of L: 6 μm; Median of NL and NLS: 4 μm). Considering all directions, the residuals ranged between −80μm and 58 μm.

3.3. Spatial distribution of residuals

At $Step_{El}$, the spatial distribution of the residuals of all three simulation methods was similar and showed concentrated regions of high absolute residuals in all directions and for most specimens (see Fig. 8 (a)). At $Step_{Ult}$, the concentrated regions of high absolute errors were similar to those recognized at the elastic load step (see Fig. 8 (b)). The simulation method L showed higher maximum absolute residuals than NL and NLS in y- and z-direction (e. g. L in z-direction max. between 46% and 104% of average compression vs. NL in z-direction max. between 29% and 91% of average compression (see Appendix B)). Fig. 8 shows the described observations for one representative sample and one displacement field direction. The results were similar for most samples and spatial directions; only the locations of high absolute residuals were different (see supplementary material).

3.4. RMSE

At $Step_{El}$, RMSE values for all specimens ranged between 2 μm and 10 μm (mean of all spatial directions: 4.5 μm) for all simulation methods and in all directions and for the magnitude (see Fig. 9 $Step_{El}$). The RMSE difference between the L and NL simulation method was lower than 0.6 μm for all specimens and in all directions and for the magnitude. NL and NLS performed quite similar.

For all three simulation methods the RMSE increased at $Step_{Ult}$, but the increase was more pronounced for the L method (see Fig. 9 $Step_{Ult}$). RMSE of L ranged between 11 μm and 18 μm in z-direction, while the reached RMSE values for the NL and NLS methods were between 8 μm and 14 μm. In x- and y-direction the difference between the L and NL method at the ultimate load step was less pronounced than in z-direction and for the magnitude.

3.5. Damage

At $Step_{Ult}$, the number of damaged elements was highest for the L simulation method (average of 11.3% of total element number). The simulation methods NL and NLS reached a far lower number of damaged elements (average of 7.4% for NL and 8.4% for NLS of total element number) (see Fig. 10 (a) and 11). Especially specimens D2 and D5 (>12.3% and 11.6% of total element number) had a high number of damaged elements. Fig. 11 (b) shows the difference in damage between

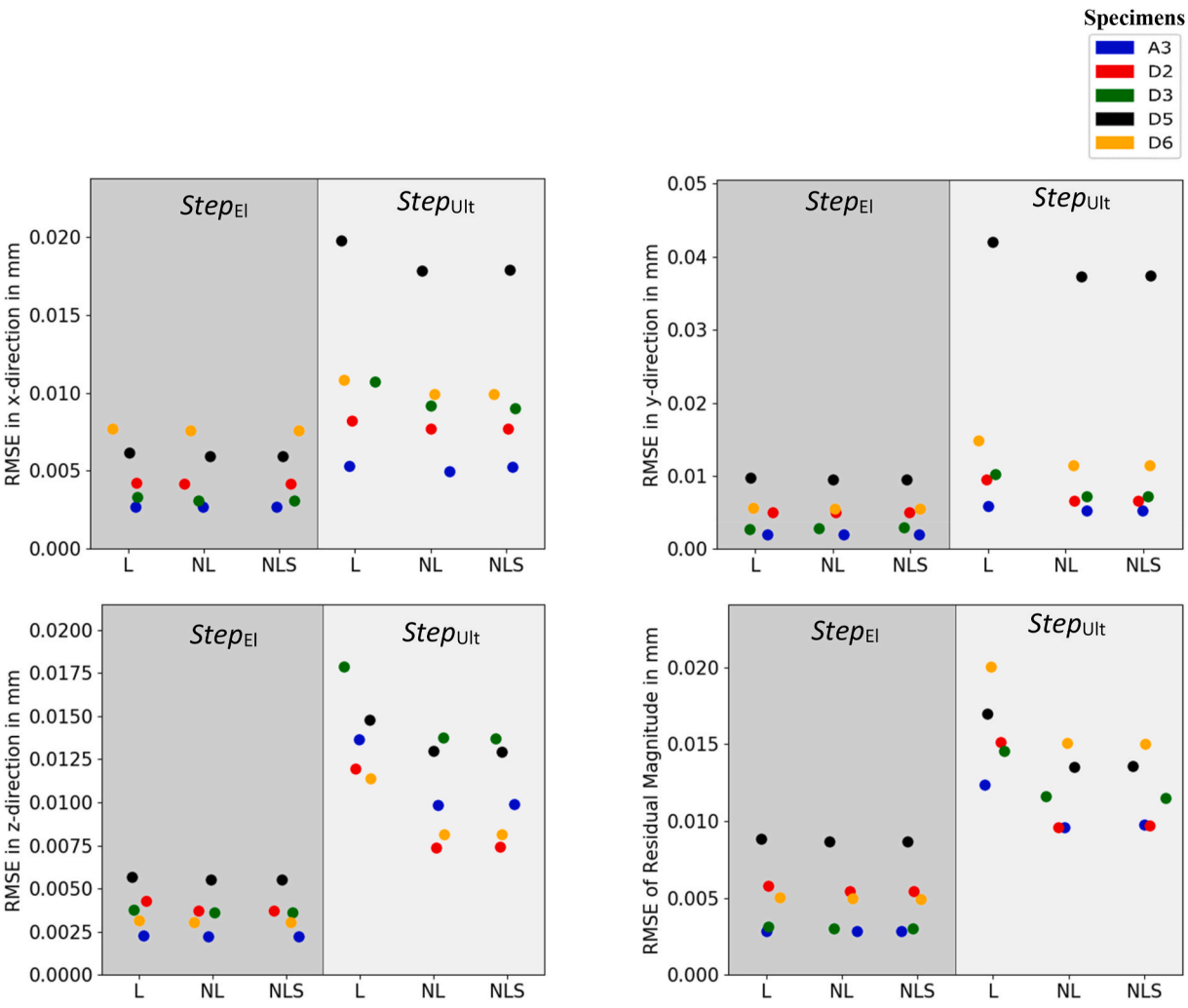

Fig. 9. RMSE of all specimens (A3, D2, D3, D5, D6) at the elastic and at the ultimate load step in all directions and for the magnitude.

the three simulations methods. The percentage of elements that were classified as damaged in the one simulation method and classified as not damaged in the other one, ranged between 1.4% and 9.8% of the total element number when L was compared to NL or NLS. Between NL and NLS the difference in damage classification was rather low (0.3%–1.6% of total element number).

The damage distribution was different for all specimens (see Fig. 11). The L simulation method overestimated the number of damaged elements, but the location of the damaged elements qualitatively agreed in all methods. The damaged region predicted by the NL method was mostly a subset of the damaged region predicted by the L method. The number of damaged elements predicted exclusively be the NL method was rather low. NL and NLS methods showed almost no differences in the damage distribution (see supplementary material).

The damage evolution (see Fig. 12 for specimen A3 and supplementary material for further specimens) showed that the number of damaged elements increased in a similar manner for NL and NLS for all specimens. The number of damaged elements was rather low until a strain value of approximately 0.4% was reached. Then the number of damaged elements increased in a linear manner.

4. Discussion

The aim of this study was to compare the displacement predictions of three μFE simulation methods (L, NL, and NLS) with DVC measurements at the elastic and in the ultimate load step. Therefore, μFE models of human trabecular bone biopsies simulating stepwise compression were analyzed, displacement predictions were averaged and compared to DVC displacement measurements of the same volume.

The results showed that all three simulation methods were able to replicate the averaged displacement field at the elastic as well as at the ultimate load step (see Fig. 6 and supplementary material). At the elastic load step, the μFE models were able to predict more than 83% of the displacement variations in all three spatial directions and for the magnitude, for all simulation methods and for all five individual specimens. At the ultimate load step, the coefficients of determination decreased but the predictions were still highly correlated to the DVC measurements.

While all three simulation methods showed similar performance regarding all evaluated parameters at the elastic load step, slight differences became evident when displacement results were evaluated at the ultimate load step. Whereas the simulation method L was able to predict more than 59% of displacement variations in all three Cartesian directions and for the magnitude, the displacements predicted by the simulation methods NL and NLS correlated better (R^2>0.68) with the DVC measured displacements (see Table 3 and supplementary material). In all directions and for all specimens the coefficient of determination was lower for the L simulation method. Furthermore, higher IQR, residual ranges, and RMSE values were observed in all directions (see Figs. 7 and 9). Similar results were reported by Peña Fernández et al. (2022) who showed that nonlinear μFE models could improve the displacement predictions in yielded bone regions. The improved

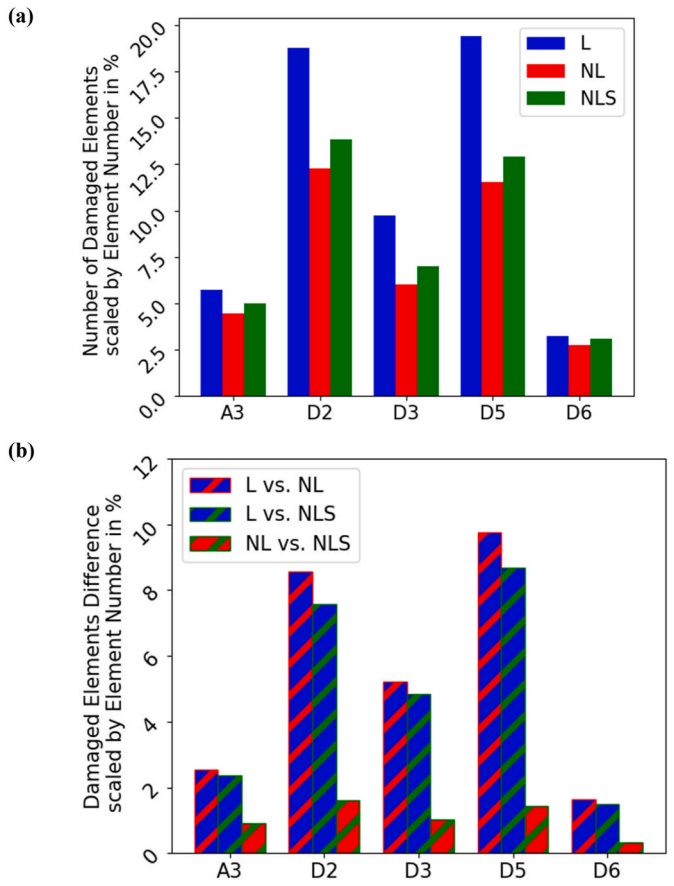

Fig. 10. (a) Number of damaged elements for all simulation methods scaled by the element number of bone material of each specimen at $Step_{Ult}$. Regarding L, elements were classified as damaged when $\varepsilon_{eff} > 0.89\%$. For the simulation methods NL and NLS, elements were classified as damaged when $D > 0$. **(b)** Difference in damage scaled by the element number of bone material of each specimen at $Step_{Ult}$. This plot visualizes the number of elements which are classified as damaged in one simulation method and classified as not damaged in the other one.

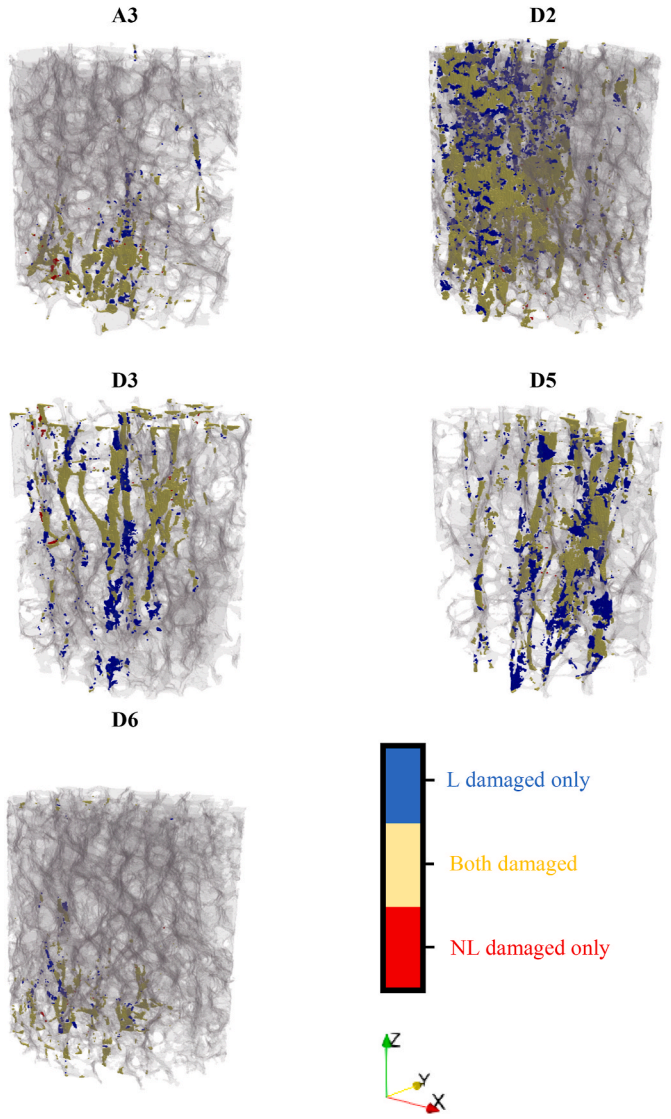

Fig. 11. Comparison of damage distribution between the simulation methods L and NL for all specimens at $Step_{Ult}$. Regarding L, elements were classified as damaged when $\varepsilon_{eff} > 0.89\%$. For the simulation methods NL and NLS, elements were classified as damaged when $D > 0$. Elements that were marked as damaged in both simulation methods are visualized in yellow, while those that only one simulation method classified as damaged were marked in blue (only L) and red (only NL).

performance in displacement prediction of the NL method at the ultimate load step was compromised by the long solving time in comparison to the L method (maximum CPU hours at $Step_{Ult}$: L: 1.1h vs. NL: 98.5h) (see Table 2). Since the L method was still capable to predict the displacement field with acceptable accuracy and precision until the ultimate load, its application seems to be sufficient when evaluating displacement fields and qualitatively evaluating damage locations of similar bone biopsies under compression. However, note that the damaged regions were found to be at similar locations but generally overestimated in L when compared to the NL or NLS methods (see Figs. 10 and 11). Thus, caution is warranted if damage is interpreted using linear μFE models at ultimate load. These results are in line with those of Stipsitz et al. (2021), where damage of linear and nonlinear μFE model simulations was observed at similar locations in the distal radius and the number of damaged elements was generally overestimated using the linear μFE models. Neither at the elastic load step nor at the ultimate load step, a difference in performance between NL and NLS could be observed. Furthermore, the number and location of damaged elements at the ultimate load step were in good agreement (see Figs. 10 and 11). In contrast, the simulation time for NLS (maximum CPU hours at $Step_{Ult}$: 230.8h) was much higher than for NL (see Table 2). One can assume that in the presented use case (small trabecular biopsy), the nonlinearity of the boundary conditions does not play a crucial role for the accuracy and precision of the local displacement field. This was also confirmed by the damage evolution, which showed only minor differences between NL and NLS (see Fig. 12). However, differences between NL and NLS could be more pronounced for different case studies (e.g. larger displacements, larger bone samples, different material models, and different output parameters) which would justify the higher computational effort.

The μFE displacement predictions of all simulation methods were better at the elastic load step. For all specimens and in all directions higher R^2 values (e.g. pooled data of NL method in z-direction: $Step_{El}$: $R^2 = 0.98$; $Step_{Ult}$: $R^2 = 0.97$), lower IQR, residual ranges (e.g. pooled data of NL method in z-direction: $Step_{El}$: -17 μm–17 μm; $Step_{Ult}$: -51 μm–41 μm), and RMSE values were observed. Damage analysis at the ultimate load step showed that the damage distribution of most specimens (A3, D2, D6) corresponded to regions of high residual errors (see Fig. 11 and supplementary material), indicating difficulties to predict the behaviour of yielding bone. Future studies could try to improve the μFE performance especially at the ultimate load step possibly by implementing a more complex material model to the simple damage-based material model that was used in this study. This suggestion is supported by Peña

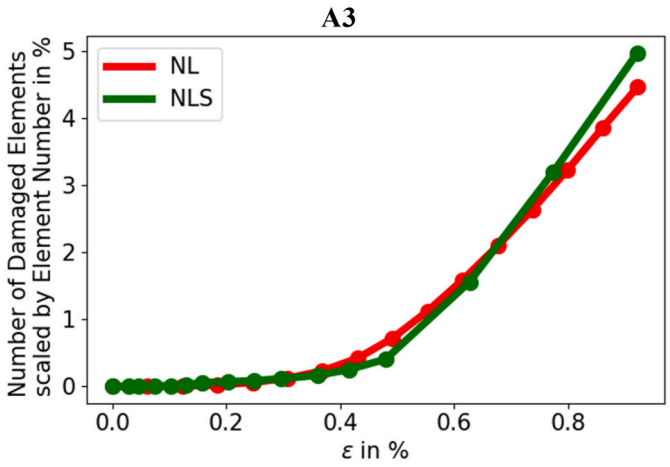

Fig. 12. Damage evolution with apparent strain ε in z-direction (for specimen cropped to middle 80% of height) for on representative specimen (A3) for simulation methods NL and NLS. For the simulation methods NL and NLS, elements were classified as damaged when $D > 0$. The y-axis shows the number of damaged elements scaled by the total element number of bone material.

Fernández et al. (2022), who used a linear elastic-viscoplastic damage model including geometrical nonlinearity and only reported minor deterioration in displacement predictions when comparing results at 1% and 3% compression. In consequence, further enhancements in material modelling are important to increase the accuracy of displacement predictions. A further approach to improve the displacement predictions of μFE models seems to be the implementation of tissue heterogeneity. However, since studies from Peña Fernández et al. (2022) and Fu et al. (2021) only reported negligible difference between homogeneous and heterogeneous models one can conclude that the microstructure dominates the mechanical behaviour of bone tissue.

The study results were generally in line with values reported in literature. At the elastic load step, the results of all evaluated parameters (regression, residuals, and RMSE) were similar to the findings reported by Costa et al. (2017) and Chen et al. (2017), who conducted similar studies with comparable GS (500 μm–1872 μm). They reported agreements of more than 86% between the displacement fields measured with DVC and predicted by linear μFE. In this study, only one specimen (D5) showed a slightly lower coefficient of determination (L: $R^2 = 0.83$) in x-direction. The RMSE value range of this study (2 μm–10 μm) was similar to that reported by Costa et al. (2017) (1 μm–12 μm) and Chen et al. (2017) (1 μm–11 μm). The results at the elastic load step were further compared to the results of Peña Fernández et al. (2022) at 1% compression. The nonlinear models showed a weaker correlation (R^2>0.53) but also smaller RMSE values below 1.7 μm than this study reported (NL: R^2>0.85; RMSE<9.5 μm). The low RMSE value can be attributed to the high resolution of 5 μm used in the study of Peña Fernández et al. (2022). The results at the ultimate load step were compared to Oliviero et al. (2018), who used a linear-elastic material model to predict the displacement fields in the elastic and in the nonlinear regime. Coefficients of determination were higher (R^2>0.77) than in this study (R^2>0.59), but RMSE values were in line with the findings of our study (e.g. Oliviero et el. (2018) in z-direction: 6 μm–24 μm; this study L method in z-direction: 11 μm–18 μm). Reasons for the weaker correlation could be that no outliers were removed, whereas in all above mentioned studies Cook's distance was applied for this purpose. In addition, the usage of the volume averaging method leads to an increased number of comparison points, including points in regions with low BV/TV and higher residuals (see Appendix A).

The study is restricted by several limitations. To begin with, the sample size was rather small, but still comparable to similar studies (Chen et al., 2017; Costa et al., 2017). Next, the study only compared averaged displacements of 1 mm^3 seized cubic volumes and did not capture local displacements. Furthermore, the displacement precision of the DVC measurements and therefore also the GS size were derived just from literature (Knowles et al., 2019; Kusins et al., 2019; Tozzi et al., 2016) and could not be evaluated with a repeated-scan test (Dall'Ara et al., 2014; Liu and Morgan, 2007) in this study. Although a direct comparison with literature would require the same bone structure and scanning parameters, previous studies evaluating precision showed that displacement errors are rather small in the size of a fraction of a voxel (Dall'Ara et al., 2014, 2017; Palanca et al., 2015). Thus, it can be assumed that they did not affect the main outcomes of this study. Nevertheless, the strain precision is much more sensitive to the image quality (signal to noise ratio) due to the fact that the differentiation process amplifies the errors associated to the displacements (Dall'Ara et al., 2017). Higher resolution images, using Synchrotron tomography (Palanca et al., 2017) would lead to a DVC accuracy high enough to compare DVC and μFE strains. However, in situ mechanical testing combined with Synchrotron tomography has limitations in assessing the local mechanical behaviour of bone tissue due to radiation induced damage (Barth et al., 2010, 2011; Singhal et al., 2011). In consequence, our study is limited to the sole evaluation of displacements and not strains. Furthermore, radiation-induced material changes or damage due to the multiple scanning of the specimens could have an influence on our study results. Nevertheless, effects of radiation were found only when higher imaging flux, typical of synchrotron μCT imaging were used (Barth et al., 2010). Although future studies need to quantify the effect of this limitation, we can assume that it did not severely compromise our study results since the displacement comparison between the μFE model and the experiments showed high correlations. Another limitation is the number of displacement steps and the variable displacement step size, which could influence the performance of the NLS method. Nevertheless, the applied displacement step size appeared sufficient to capture the nonlinearity in the apparent load-displacement curves. Lastly, the application of the highly parallel μFE solver ParOSol comes with the limitation that geometrical nonlinearity and further aspects of the constitutive behaviour of bone material (plasticity, viscosity, poroelasticity) were not considered. However, the usage of ParOSol together with its implemented damage-based material model can be justified since the solver works highly efficient and therefore enables to simulate large bone structures.

5. Conclusions

In this study, predicted displacements of linear and nonlinear μFE models were compared to DVC measured displacements at a specific load step in the elastic regime and at the ultimate load step. The predicted displacement fields of all μFE simulation methods were in good agreement with the DVC measured displacement fields. Although the nonlinear μFE models improved the prediction of the displacement fields slightly at the ultimate load step in all spatial directions, the increased simulation times cannot be ignored. Furthermore, damage was evaluated and occurred at similar locations for all linear and nonlinear μFE models. Hence, this study confirms that for similar use cases (displacement and qualitative damage evaluation of compressed trabecular bone biopsies) linear μFE models are sufficient in order to predict displacement fields in the linear and nonlinear regime as well as to reveal damage locations with acceptable accuracy and very low computational effort.

CRediT authorship contribution statement

Pia Stefanek: Writing – original draft, Project administration, Investigation, Formal analysis. **Alexander Synek:** Writing – review & editing, Supervision, Methodology, Conceptualization. **Enrico Dall'Ara:** Writing – review & editing, Supervision, Software, Methodology. **Dieter H. Pahr:** Writing – review & editing, Supervision, Methodology, Conceptualization.

Declaration of competing interest

The authors declare the following financial interests/personal relationships which may be considered as potential competing interests: DP is CEO of Dr. Pahr Ingenieurs e.U. which develops and distributes the software Medtool. PS, AS and ED have no conflicts of interest to declare.

Data availability

Data will be made available on request.

Acknowledgements

This research did not receive any specific grant from funding agencies in the public, commercial, or not-for-profit sectors. The authors acknowledge TU Wien Bibliothek for financial support through its Open Access Funding Program.

Appendix C. Supplementary data

Supplementary data to this article can be found online at https://doi.org/10.1016/j.jmbbm.2022.105631.

Appendix A

The majority of studies that compared µFE results to DVC measurements used a pointwise validation (Chen et al., 2017; Costa et al., 2017; Oliviero et al., 2018; Palanca et al., 2022). The pointwise method only includes DVC points inside the µFE mesh. Since the DVC nodes are by construction located at the center of the µFE elements, the DVC displacement values were compared to the interpolated displacement values of the µFE nodes. Fig. A.1 compares the two different evaluation methods (volume-averaging vs. pointwise) at $Step_{El}$ and $Step_{Ult}$ for one representative specimen in z-direction for the simulation method L. The results for intercept, slope, and R^2 are quite similar for both methods. A difference between the evaluation methods is the number of comparison points (Volume-averaging method: 476 points; Pointwise method: 83 points).

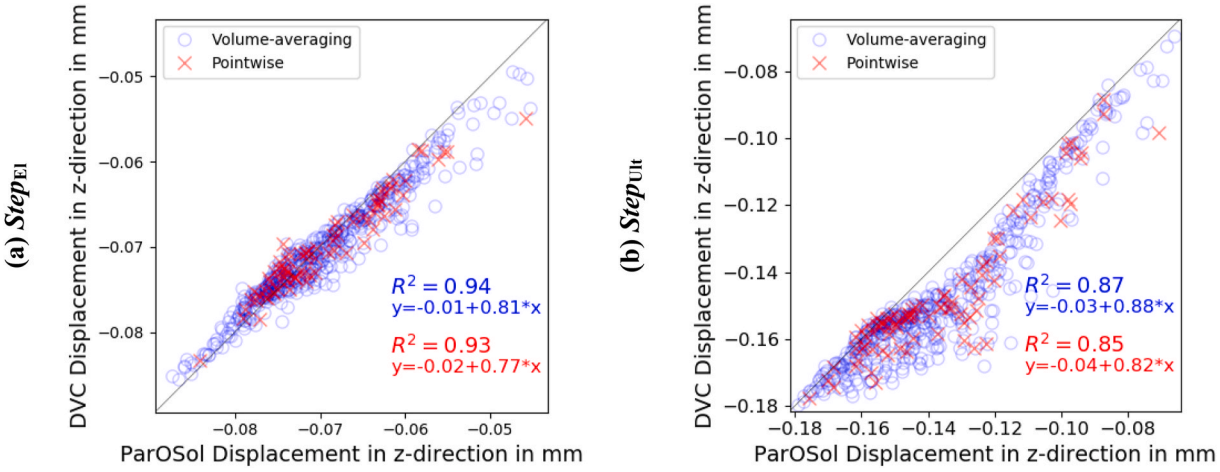

Fig. A.1. Comparison of evaluation methods at the elastic (a) and at the ultimate (b) load step for one representative specimen (A3) in z-direction using the linear simulation method.

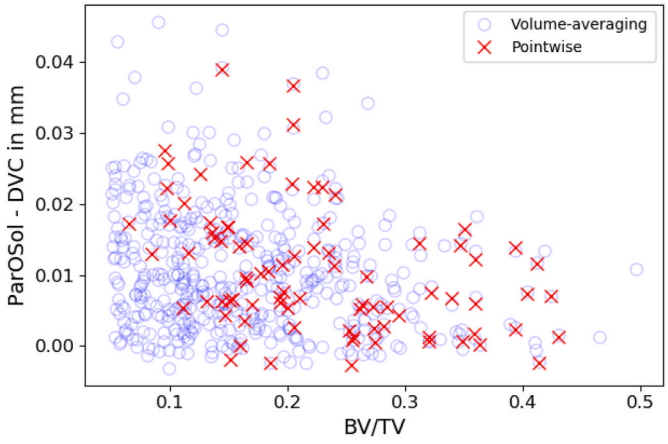

Fig. A.2. Comparison points of the evaluation methods regarding BV/TV of the surrounding cubic volume and residual height at $Step_{Ult}$. One representative specimen (A3) was selected and evaluated with the linear simulation method in z-direction.

Furthermore, Fig. A.2 shows another difference between the evaluation methods. Most comparison points of the pointwise method refer to cubic volumes with a BV/TV of more than 10%. Regarding the volume-averaging method, there are many comparison points that refer to cubic volumes with a low BV/TV between 5 and 10%. Moreover, Fig. A.2 shows that the residual values are higher in volumes of low BV/TV. The results were similar

for all specimens, all simulation methods and in all directions.

Appendix B

Depending on the evaluated load step ($Step_{El}$, $Step_{Ult}$), the average compression of the individual specimens was computed in the following way:

$$\Delta^{DVC}\underline{u} = {}^{DVC}\underline{u}_{Top} - {}^{DVC}\underline{u}_{Bottom} \tag{B.1}$$

${}^{DVC}\underline{u}_{Top}$ describes the average DVC displacement at the top layer of the comparison region (64% of orginal specimen height). Equally, ${}^{DVC}\underline{u}_{Bottom}$ describes the average DVC displacement at the bottom layer of the comparison region.

References

Barth, H.D., Launey, M.E., MacDowell, A.A., Ager, J.W., Ritchie, R.O., 2010. On the effect of X-ray irradiation on the deformation and fracture behavior of human cortical bone. Bone 46 (6), 1475–1485. https://doi.org/10.1016/j.bone.2010.02.025.

Barth, H.D., Zimmermann, E.A., Schaible, E., Tang, S.Y., Alliston, T., Ritchie, R.O., 2011. Characterization of the effects of x-ray irradiation on the hierarchical structure and mechanical properties of human cortical bone. Biomaterials 32 (34), 8892–8904. https://doi.org/10.1016/j.biomaterials.2011.08.013.

Bevill, G., Keaveny, T.M., 2009. Trabecular bone strength predictions using finite element analysis of micro-scale images at limited spatial resolution. Bone 44 (4), 579–584. https://doi.org/10.1016/j.bone.2008.11.020.

Boyd, S.K., 2009. Image-based finite element analysis. In: Advanced Imaging in Biology and Medicine: Technology, Software Environments, Applications, pp. 301–318.

Chen, Y., Dall'Ara, E., Sales, E., Manda, K., Wallace, R., Pankaj, P., Viceconti, M., 2017. Micro-CT based finite element models of cancellous bone predict accurately displacement once the boundary condition is well replicated: a validation study. J. Mech. Behav. Biomed. Mater. 65, 644–651. https://doi.org/10.1016/j.jmbbm.2016.09.014.

Christen, D., Melton, L.J., Zwahlen, A., Amin, S., Khosla, S., Müller, R., 2013. Improved fracture risk assessment based on nonlinear micro-finite element simulations from HRpQCT images at the distal radius. J. Bone Miner. Res. 28 (12), 2601–2608. https://doi.org/10.1002/jbmr.1996.

Cody, D.D., Gross, G.J., Hou, F.J., Spencer, H.J., Goldstein, S.A., Fyhrie, D.P., 1999. Femoral strength is better predicted by finite element models than QCT and DXA. J. Biomech. 32, 1013–1020.

Costa, M.C., Tozzi, G., Cristofolini, L., Danesi, V., Viceconti, M., Dall'Ara, E., 2017. Micro finite element models of the vertebral body: validation of local displacement predictions. PLoS One 12 (7), 1–18. https://doi.org/10.1371/journal.pone.0180151.

Dall'Ara, E., Barber, D., Viceconti, M., 2014. About the inevitable compromise between spatial resolution and accuracy of strain measurement for bone tissue: a 3D zero-strain study. J. Biomech. 47 (12), 2956–2963. https://doi.org/10.1016/j.jbiomech.2014.07.019.

Dall'Ara, E., Peña-Fernández, M., Palanca, M., Giorgi, M., Cristofolini, L., Tozzi, G., 2017. Precision of digital volume correlation approaches for strain analysis in bone imaged with micro-computed tomography at different dimensional levels. Frontiers in Materials 4. https://doi.org/10.3389/fmats.2017.00031.

Ding, H., Zhu, Z.A., Dai, K.R., Ye, M., Wang, C.T., 2008. Research on damage in trabecular bone of the healthy human acetabulum at small strains using nonlinear micro-finite element analysis. J. Shanghai Jiaot. Univ. 13 E (5), 623–628. https://doi.org/10.1007/s12204-008-0623-5.

Flaig, C., Arbenz, P., 2012. A highly scalable matrix-free multigrid solver for μFE analysis based on a pointer-less octree. Large-Scale Sci. Comput. 498–506.

Fu, J., Meng, H., Zhang, C., Liu, Y., Chen, D., Wang, A., Main, R.P., Yang, H., 2021. Effects of tissue heterogeneity on trabecular micromechanics examined by microCT-based finite element analysis and digital volume correlation. Med. Novel Technol. Dev. 11, 100088 https://doi.org/10.1016/j.medntd.2021.100088.

Hosseini, H.S., Horák, M., Zysset, P.K., Jirásek, M., 2015. An over-nonlocal implicit gradient-enhanced damage-plastic model for trabecular bone under large compressive strains. Int. J. Numer. Methods Biomed. Eng. 31 (11), 32. https://doi.org/10.1002/cnm.2728.

Jackman, T.M., DelMonaco, A.M., Morgan, E.F., 2016. Accuracy of finite element analyses of CT scans in predictions of vertebral failure patterns under axial compression and anterior flexion. J. Biomech. 49 (2), 267–275. https://doi.org/10.1016/j.jbiomech.2015.12.004.

Knowles, N.K., Kusins, J., Faieghi, M., Ryan, M., Dall'Ara, E., Ferreira, L.M., 2019. Material mapping of QCT-derived scapular models: a comparison with micro-CT loaded specimens using digital volume correlation. Ann. Biomed. Eng. 47 (11), 2188–2198. https://doi.org/10.1007/s10439-019-02312-2.

Kusins, J., Knowles, N., Ryan, M., Dall'Ara, E., Ferreira, L., 2019. Performance of QCT-Derived scapula finite element models in predicting local displacements using digital volume correlation. J. Mech. Behav. Biomed. Mater. 97, 339–345. https://doi.org/10.1016/j.jmbbm.2019.05.021.

Liu, L., Morgan, E.F., 2007. Accuracy and precision of digital volume correlation in quantifying displacements and strains in trabecular bone. J. Biomech. 40 (15), 3516–3520. https://doi.org/10.1016/j.jbiomech.2007.04.019.

Madi, K., Tozzi, G., Zhang, Q.H., Tong, J., Cossey, A., Au, A., Hollis, D., Hild, F., 2013. Computation of full-field displacements in a scaffold implant using digital volume correlation and finite element analysis. Med. Eng. Phys. 35 (9), 1298–1312. https://doi.org/10.1016/j.medengphy.2013.02.001.

Martelli, S., Giorgi, M., Dall' Ara, E., Perilli, E., 2021. Damage tolerance and toughness of elderly human femora. Acta Biomater. 123, 167–177. https://doi.org/10.1016/j.actbio.2021.01.011.

Müller, R., 2009. Hierarchical microimaging of bone structure and function. Nat. Rev. Rheumatol. 5 (7), 373–381. https://doi.org/10.1038/nrrheum.2009.107.

Niebur, G.L., Feldstein, M.J., Yuen, J.C., Chen, T.J., Keaveny, T.M., 2000. High-resolution finite element models with tissue strength asymmetry accurately predict failure of trabecular bone. J. Biomech. 33.

Oliviero, S., Giorgi, M., Dall'Ara, E., 2018. Validation of finite element models of the mouse tibia using digital volume correlation. J. Mech. Behav. Biomed. Mater. 86, 172–184. https://doi.org/10.1016/j.jmbbm.2018.06.022.

Ovesy, M., Indermaur, M., Zysset, P.K., 2019. Prediction of insertion torque and stiffness of a dental implant in bovine trabecular bone using explicit micro-finite element analysis. J. Mech. Behav. Biomed. Mater. 98, 301–310. https://doi.org/10.1016/j.jmbbm.2019.06.024.

Pahr, D.H., Reisinger, A.G., 2020. A review on recent advances in the constitutive modeling of bone tissue. Curr. Osteoporos. Rep. 18 (6), 696–704. https://doi.org/10.1007/s11914-020-00631-1.

Palanca, M., Bodey, A.J., Giorgi, M., Viceconti, M., Lacroix, D., Cristofolini, L., Dall'Ara, E., 2017. Local displacement and strain uncertainties in different bone types by digital volume correlation of synchrotron microtomograms. J. Biomech. 58, 27–36. https://doi.org/10.1016/j.jbiomech.2017.04.007.

Palanca, M., de Donno, G., Dall'Ara, E., 2021. A novel approach to evaluate the effects of artificial bone focal lesion on the three-dimensional strain distributions within the vertebral body. PLoS One 16 (6 June). https://doi.org/10.1371/journal.pone.0251873.

Palanca, M., Oliviero, S., Dall'Ara, E., 2022. MicroFE models of porcine vertebrae with induced bone focal lesions: validation of predicted displacements with digital volume correlation. J. Mech. Behav. Biomed. Mater. 125 https://doi.org/10.1016/j.jmbbm.2021.104872.

Palanca, M., Tozzi, G., Cristofolini, L., Viceconti, M., Dall'Ara, E., 2015. Three-dimensional local measurements of bone strain and displacement: comparison of three digital volume correlation approaches. J. Biomech. Eng. 137 (7) https://doi.org/10.1115/1.4030174.

Peña Fernández, M., Sasso, S.J., McPhee, S., Black, C., Kanczler, J., Tozzi, G., Wolfram, U., 2022. Nonlinear micro finite element models based on digital volume correlation measurements predict early microdamage in newly formed bone. J. Mech. Behav. Biomed. Mater. 132, 105303 https://doi.org/10.1016/j.jmbbm.2022.105303.

Rho, J.-Y., Kuhn-Spearing, L., Zioupos, P., 1998. Mechanical properties and the hierarchical structure of bone. Med. Eng. Phys. 20, 92–102.

Ruffoni, D., van Lenthe, G.H., 2011. Finite element analysis in bone research: a computational method relating structure to mechanical function. Compr. Biomater. 3 (October), 91–111. https://doi.org/10.1016/b978-0-12-803581-8.09798-8.

Ryan, M.K., Oliviero, S., Costa, M.C., Mark Wilkinson, J., Dall'ara, E., 2020. Heterogeneous strain distribution in the subchondral bone of human osteoarthritic femoral heads, measured with digital volume correlation. Materials 13 (20), 1–18. https://doi.org/10.3390/ma13204619.

Sabet, F.A., Jin, O., Koric, S., Jasiuk, I., 2018. Nonlinear micro-CT based FE modeling of trabecular bone—sensitivity of apparent response to tissue constitutive law and bone volume fraction. Int. J. Numer. Methods Biomed. Eng. 34 (4) https://doi.org/10.1002/cnm.2941.

Sabet, F.A., Najafi, A.R., Hamed, E., Jasiuk, I., 2016. Modelling of bone fracture and strength at different length scales: a review. In: Interface Focus. Royal Society of London. https://doi.org/10.1098/rsfs.2015.0055. Vol. 6, Issue 1.

Schwiedrzik, J., Gross, T., Bina, M., Pretterklieber, M., Zysset, P., Pahr, D., 2016. Experimental validation of a nonlinear μFE model based on cohesive-frictional plasticity for trabecular bone. Int. J. Numer. Methods Biomed. Eng. 32 (4) https://doi.org/10.1002/cnm.2739.

Singhal, A., Deymier-Black, A.C., Almer, J.D., Dunand, D.C., 2011. Effect of high-energy X-ray doses on bone elastic properties and residual strains. J. Mech. Behav. Biomed. Mater. 4 (8), 1774–1786. https://doi.org/10.1016/j.jmbbm.2011.05.035.

Stipsitz, M., Pahr, D.H., 2018. AN efficient solver for large-scale simulations of voxel-based structures using a nonlinear damage. MATERIAL MODEL (Issue 7). https://www.ilsb.tuwien.ac.at.

Stipsitz, M., Zysset, P.K., Pahr, D.H., 2020. Efficient materially nonlinear μFE solver for simulations of trabecular bone failure. Biomech. Model. Mechanobiol. 19 (3), 861–874. https://doi.org/10.1007/s10237-019-01254-x.

Stipsitz, M., Zysset, P.K., Pahr, D.H., 2021. Prediction of the inelastic behaviour of radius segments: damage-based nonlinear micro finite element simulation vs pistoia criterion. J. Biomech. 116 https://doi.org/10.1016/j.jbiomech.2020.110205.

Taylor, R.L., 2014. FEAP - Finite Element Analysis Program. University of California, Berkeley. http://www.ce.berkeley/feap.

Tozzi, G., Dall'Ara, E., Palanca, M., Curto, M., Innocente, F., Cristofolini, L., 2017. Strain uncertainties from two digital volume correlation approaches in prophylactically augmented vertebrae: local analysis on bone and cement-bone microstructures. J. Mech. Behav. Biomed. Mater. 67, 117–126. https://doi.org/10.1016/j.jmbbm.2016.12.006.

Tozzi, G., Danesi, V., Palanca, M., Cristofolini, L., 2016. Elastic full-field strain analysis and microdamage progression in the vertebral body from digital volume correlation. Strain 52 (5), 446–455. https://doi.org/10.1111/str.12202.

van Rietbergen, B., Ito, K., 2015. A survey of micro-finite element analysis for clinical assessment of bone strength: the first decade. J. Biomech. 48 (5), 832–841. https://doi.org/10.1016/j.jbiomech.2014.12.024.

van Rietbergen, B., Weinans, H., Huiskes, R., Odgaardt, A., 1995. A new method to determine trabecular bone elastic properties and loading using micromechanical finite-element models. J. Biomech. 28 (1), 69–81.

Verhulp, E., van Rietbergen, B., Müller, R., Huiskes, R., 2008. Micro-finite element simulation of trabecular-bone post-yield behaviour - effects of material model, element size and type. Comput. Methods Biomech. Biomed. Eng. 11 (4), 389–395. https://doi.org/10.1080/10255840701848756.

Virtanen, P., Gommers, R., Oliphant, T.E., Haberland, M., 2020. SciPy 1.0: fundamental algorithms for scientific computing in Python. Nat. Methods 17 (3), 261–272.

Wolfram, U., Wilke, H.J., Zysset, P.K., 2010. Valid μ finite element models of vertebral trabecular bone can be obtained using tissue properties measured with nanoindentation under wet conditions. J. Biomech. 43 (9), 1731–1737. https://doi.org/10.1016/j.jbiomech.2010.02.026.

Yan, L., Cinar, A., Ma, S., Abel, R., Hansen, U., Marrow, T.J., 2020. A method for fracture toughness measurement in trabecular bone using computed tomography, image correlation and finite element methods. J. Mech. Behav. Biomed. Mater. 109 https://doi.org/10.1016/j.jmbbm.2020.103838.

Yeh, O.C., Keaveny, T.M., 2001. Relative roles of microdamage and microfracture in the mechanical behavior of trabecular bone. J. Orthop. Res. 19, 1001–1007. www.elsevier.com/locate/orthres.

Zauel, R., Yeni, Y.N., Bay, B.K., Dong, X.N., Fyhrie, D.P., 2006. Comparison of the linear finite element prediction of deformation and strain of human cancellous bone to 3D digital volume correlation measurements. J. Biomech. Eng. 128 (1), 1–6. https://doi.org/10.1115/1.2146001.